The Cell Cooling Coefficient: A Standard to Define Heat Rejection from Lithium-Ion Batteries

Alastair Hales, [●][1] Laura Bravo Diaz, [●][1] Mohamed Waseem Marzook,[●][1] Yan Zhao,[●][1] Yatish Patel, [●][1] and Gregory Offer [●][1,2,*,z]

[1]*Department of Mechanical Engineering, Imperial College London, London SW7 2AZ, United Kingdom*
[2]*The Faraday Institution, Quad One, Harwell Science and Innovation Campus, Didcot, United Kingdom*

Lithium-ion battery development is conventionally driven by energy and power density targets, yet the performance of a lithium-ion battery pack is often restricted by its heat rejection capabilities. It is therefore common to observe elevated cell temperatures and large internal thermal gradients which, given that impedance is a function of temperature, induce large current inhomogeneities and accelerate cell-level degradation. Battery thermal performance must be better quantified to resolve this limitation, but anisotropic thermal conductivity and uneven internal heat generation rates render conventional heat rejection measures, such as the Biot number, unsuitable. The Cell Cooling Coefficient (CCC) is introduced as a new metric which quantifies the rate of heat rejection. The CCC (units W.K^{-1}) is constant for a given cell and thermal management method and is therefore ideal for comparing the thermal performance of different cell designs and form factors. By enhancing knowledge of pack-wide heat rejection, uptake of the CCC will also reduce the risk of thermal runaway. The CCC is presented as an essential tool to inform the cell down-selection process in the initial design phases, based solely on their thermal bottlenecks. This simple methodology has the potential to revolutionise the lithium-ion battery industry.

Lithium-ion batteries (LIBs) are becoming increasingly important for ensuring sustainable mobility and a reliable energy supply in the future, due to major concerns regarding air quality, greenhouse gas emissions and energy security.[1–3] One of the major challenges of using LIBs in demanding applications such as hybrid and electric vehicles is thermal management, as cells generate a considerable amount of heat during operation.[4–8] If this heat is not removed efficiently then cell temperatures increase which accelerates degradation.[9–13] However, removing the heat creates thermal gradients within cells due to the finite and anisotropic thermal conductivity. The impedance of a cell is a strong function of temperature, and therefore thermal gradients cause different regions to have different impedances which results in current inhomogeneities.[14] The consequence is accelerated and varying rates of degradation, observed between layers within a cell[15,16] and between cells in a pack.[17] Counterintuitively, the contribution of these thermal gradients to degradation can sometimes be larger than the effect of higher average absolute temperatures.[14]

Considerable improvements in battery lifetime, through the design of better thermal management systems, is essential for innovation in the field.[15] However, the impact of internal thermal gradients is rarely considered in cell design. Cell heat generation and heat rejection pathways are often overlooked, power and energy density are optimised instead. However, a badly designed cell from a thermal management perspective could lead to reduced power, less usable capacity and reduced energy density at pack level. Currently it is impossible without extensive modelling or testing for systems engineers to understand which cells have been designed well for thermal management from information contained on a specification sheet. There is therefore a need for a simple metric which if introduced would allow cell designers and systems engineers to evaluate cells against each other in terms of their ability to reject heat. Including this metric on cell specification sheets would have the potential to revolutionise the whole industry by making optimising cells for thermal management just as important as optimising for power and/or energy.

In this study, a new metric, the Cell Cooling Coefficient (CCC) with units of W.K^{-1}, and a standardised method of measuring it, is introduced to evaluate the thermal pathways of a cell based on its physical design. This singular metric quantifies the rate of heat rejection, through different thermal pathways within the cell geometry, as a result of internal thermal gradients. As it is independent of cell design, form factor, or internal materials, this allows comparison between different cell formats, chemistries and geometries, unachievable with present industry standard measures. A cell with a higher CCC would enable higher continuous powers to be used, with smaller thermal gradients within the cell and therefore higher usable capacity. This translates to a lower average cell temperature during operation which combined with smaller thermal gradients would lead to a longer life. This new metric should enable not only end-users, system and design engineers but also cell designers, manufacturers and developers to compete on designing cells that can be effectively thermally managed, offering significant improvements in performance, lifetime and cost at the system level.

Literature Review

Temperature is a critical factor in battery performance optimisation. For most material combinations, the suitable operating temperature range for LIBs is between 20°C–40°C. Large temperature deviations, especially during fast charging, can lead to accelerated degradation and, in extreme cases, thermal runaway.[4,5,13,18,19] Thermal gradients within LIBs and LIB thermal management have therefore become the focus of intensive research in an attempt to improve battery performance and lifespan.[14–16,20] Despite the growing research in this field, cell heat generation and heat rejection pathways are not usually considered during the cell design phase, leading to cells prone to internal thermal gradients.

Thermal gradients within a cell or between cells in a pack themselves, contribute to uneven heat generation in operation due to positive feedback.[14–17] Heat is generated within a cell during operation due to both reversible and irreversible processes at the pore-scale.[4,5,21–26] The reversible heat is dominated by the entropy change associated with material phase changes in the cell. The irreversible heat is a consequence of the losses due to the difference between the cell open-circuit potential and the operating potential and includes: 1) the ohmic heat which is related to long-range interactions (i.e. transport of charge and species in the solid and electrolyte phases) and 2) the kinetic heat, related to short-range interactions (i.e. charge-transfer reactions at the interphase).[27] The general equation evaluating the heat generation rate by a single cell as described by Bernardi et al.[28] in its simplified form is:

$$\dot{Q} = I \cdot (U_{OC} - V) - I \cdot \left(T \cdot \frac{dU_{OC}}{dT} \right) \quad [1]$$

The first term represents the irreversible heat, considering the charge transfer overpotential at the interface, ohmic heat, kinetic heat and mass transfer limitations and the second term accounts for the reversible entropic heat. The entropy coefficient in this last term (dUOC/dT) is a function of the state of charge (SOC), active material density and temperature.[29]

Several experimental methods for determining a single cell's heat generation rate are presented in the literature.[4] The most frequently referenced method is accelerated rate calorimetry, which determines heat generation by recording a cell's temperature rise over the course of a procedure in an adiabatic environment.[30–34] However, adiabatic testing does not facilitate the assessment of heat dissipation pathways. Xie et al. allowed a large pouch cell to dissipate heat via forced and free convection in a climate-control chamber.[35] Under forced convection, the convective heat transfer coefficient is not uniform across a cell surface, and consequently quantification of heat transfer rate will contain an inherent error.[15,36] Further limitations of relying upon forced convection for thermal control are evaluated in detail by Ardani et al.[37]

A thermal management system (TMS) is generally employed to remove the heat generated by the cells within a battery pack. The TMS is used to keep all the cells at an optimum operating temperature, minimising temperature differences among cells to avoid thermal gradient buildup within the pack.[6,8] The TMS design varies depending on the strategy used to cool the cells, the fluid employed as the cooling medium and how this fluid is applied to the cell.[29,34,38–40]

Forced air convection has been a common thermal management approach for cells across a range of applications,[5] i.e. 2001 model Toyota Prius fan-driven cooling system.[41] Air, however, lacks the specific heat capacity to be sufficient for the current and future generations of pure EVs.[42] This trend is exaggerated when considering pouch cells against cylindrical cells as their increased packing factor allows for greater pack power density.[43] Air cooling is now confined to low discharge rate applications.[5]

The enhanced heat capacity of liquids make them preferable for high power applications.[29] Liquid cooling systems may be split into two categories, direct (immersion) cooling and indirect (cold plate) cooling.[5] Indirect liquid cooling, compared to direct cooling with the same power, reportedly maintains a lower average temperature across the surface of a large pouch cell.[44] Furthermore, direct cooling requires the use of dielectric fluids, which have inferior thermal properties to those used in indirect systems[29] and can present safety concerns regarding fluid containment.[7]

Based on these arguments, it is logical to assume the next generation of lithium-ion cells will be cooled by conduction from a surface. Focusing on pouch cells, the pouch surface is the largest and therefore theoretically the most ideal surface to applying cooling.[45,46] Nevertheless, surface cooling has significant limitations. Hunt et al.[15] found that degradation is accelerated, induced by layer-to-layer thermal gradients, shortening the usable life of a surface cooled pouch cell by 66%, compared to an identical, tab cooled cell.[14] Further, Bazinski et al. observed reduced thermal gradients across a pouch cell surface, when active cooling was applied to the positive tab.[47] The effective thermal conductivity for layer-to-layer heat transfer (representing surface cooling) in a pouch cell has been experimentally determined to be 5.22W/m.K.[35] Heat transfer along a layer (in-layer) within the electrode-stack, meanwhile, has a thermal conductivity increased by one order of magnitude.[15,48] However, tab cooling is limited by the rate of heat removal since heat must conduct through the very small cross sectional area of a tab. Despite this, tab cooling is considered for industrial applications.[49]

Pouch cell surface cooling is almost always applied uniformly across a cell surface[7,42] and is therefore quantifiable by considering the temperature difference between cell and cooling plate, and the measurable quality of the thermal interface. By contrast, pouch cell tab cooling is dependent on multiple geometric and thermal parameters, and consequently is very difficult to quantify. The resistance to heat dissipation through the tabs is dependent on their size, thickness and material properties, whilst the magnitudes of the thermal gradients within the cell are further dependent on the tabs' positions. Samba

et al. found thermal gradients across a pouch cell (length = 230 mm; width = 150 mm) can be reduced by 41.7% when the tabs are positioned centrally on adjacent long edges, rather than symmetrically on the same short edge.[50] The two tabs of a given cell are most often dissimilar, not only geometrically, also thermally. Copper is typically used as the negative current collector whilst aluminium is preferred for the positive.[44,51] Therefore, a higher rate of heat transfer, assuming equal thermal gradients, would be expected through the negative tab.[51]

The dimensionless Biot number may be used to define a single body's ability to dissipate heat to a surface and the subsequent rejection of heat from the surface.[52] Theoretically, it describes the transient thermal conduction response to internal thermal gradients, and may be derived from Equation 2, where k_b is the thermal conductivity of the body's material, L_C is the characteristic length (most commonly the length over which conductive heat transfer is occurring) and h_s is the heat transfer coefficient of the cooled surface. The singular characteristic length dimension limits the Biot number's applicability for a body of complex topology such as a LIB. The singular thermal conductivity does not account for the composite and anisotropic nature and of a cell, nor the presence of multiple interfaces within in the cell.

$$Bi = \frac{L_C h_s}{k_b} \qquad [2]$$

Drake et al.[53] revert to the use of a thermal conductance (units W.m^{-2}.K^{-1}) to thermally characterize their cells under test. Although it is noted that the anisotropic thermal conductivity complicates thermal conductance, this problem may be alleviated by defining a thermal conductance for each dimension of heat transfer. A true thermal conductance, however, relies upon a constant cross-sectional area for conductive heat flow, which is not the case for tab cooling of pouch cells. Further, thermal conductance by definition defines a parameter for conductive heat transfer from one plane to another and does not account for complex nature of heat generation throughout the active material within the cell. The same critical analysis is made of the use of thermal resistance.[54]

A single measure which defines the rate of conductive heat transfer that is achieved to a cell's cooled surface (such as either one or both tabs), as a result of a thermal gradient from the cell's hottest point to the cooled surface, would be highly beneficial for the thermal characterization of cells. Further, the measure should not require the input of a cross-sectional area, as is the case for the conventional thermal coefficients identified. Elimination of the area metric will allow for the comparison of two geometrically dissimilar cells.

The lack of knowledge of heat rejection from a cell, given cells are often not optimised from the thermal management perspective, is leading to suboptimal cell designs and inefficient TMSs.[40] The consequence of this on the industry is unknown. Enhancing the knowledge of the tabs' thermal pathways will highlight tab cooling as an effective method for extending the life of LIBs,[15] and drive change in the designs of the next generation of cells and thermal management systems.

Aims and Objectives

This study proposes a new standard metric to evaluate the thermal pathways of a cell for tab cooling. This will quantify the cooling capacity of different cells based on their physical design, independent of their chemistry, format or geometry. This metric, the "Cell Cooling Coefficient" (CCC), can be used as a design tool for cell design and optimisation, as well as a standard to inform manufacturers of the thermal management required for a particular cell in a pack, based on the ability of the cell to reject heat. The purpose of the CCC is threefold: enhancing battery safety from the design perspective (facilitating the down-selection of cells considering their critical temperature rise and appropriate thermal management design therefore reducing the possibility of triggering thermal runaway), guiding cell design research by quantifying a cell's heat rejection capabilities, and the standardisation of cells in the context of heat rejection.

In this study, the experimental apparatus and methodology necessary for the CCC derivation is introduced. Further, two cell types are

Table I. Geometric properties of LIB A and LIB B. Each directly affects the cells' tabs as a heat rejection pathway.

Parameter	LIB A	LIB B
Cell length/mm	113.0	89.5
Cell width/mm	40.0	101.5
Cell thickness/mm	11.3	7.4
Negative tab width/mm	20.0	7.0
Negative tab thickness/mm	0.3	0.2
Positive tab width/mm	20.0	6.9
Positive tab thickness (cell side of weld)/mm	0.4	0.2
Positive tab thickness (at weld)/mm	0.6	0.4
Positive tab thickness (tab side of weld)/mm	0.2	0.2
Negative tab internal length	13.0	10.0
Positive tab internal length	13.0	10.0
Tab locations (on the cell)	Opposite ends	Same end
Negative Tab Position (width dimension)	Central	4.5 mm offset
Positive Tab Position (width dimension)	Central	30.9 mm offset
Negative Tab Position (Thickness)	Central	Fully offset
Positive Tab Position (Thickness)	Central	Fully offset

assessed and compared using the CCC metric, facilitating quantitative analysis of a specific thermal pathway. A multi-dimensional electro-thermal model is employed to approximate the internal cell temperatures that cannot be recorded during experiments. These results were used to justify the use of cell surface temperature measurements to approximate internal temperatures. The model was also used to verify heat rejection patterns observed in experimental results.

Experimental

Cell properties.—Two types of cell were used for the present investigation: a high power Kokam 5Ah lithium-ion cell (SLPB11543140H5) (LIB A) and a high energy Kokam 7.5Ah (SLPB75106100) (LIB B). Both cells use a graphite anode and a LiMnNiCoO$_2$ (NCM) cathode for LIB A, and a Li(Ni$_{0.4}$Co$_{0.6}$)O$_2$ cathode for LIB B[15,55]. Table I defines external geometric parameters of the two cells. The significance of the large geometric dissimilarities is that each individual cell geometric characteristic has a direct effect on the quality of the cell's overall capability to be effectively tab cooled. All cells used in the investigation were brand new, i.e. beginning of life.

Table II details the internal geometric and thermal properties of the same two cells.[15,55] The varying volumetric proportions of the physical materials within each layer of the electrode-stack (current collectors, electrodes and separator), which are typically not known by the end-user, have a significant effect on the cell's overall heat

rejection properties. By comparing the relative in-layer thermal conductivities, k_{eff}, which have been calculated using the presented data sourced from the literature, it is found that in-layer heat dissipation occurs, theoretically, at a 107% higher rate in LIB A.

Apparatus.—The cells were cycled according to specifically designed cycling procedure to allow the CCC value characterization. The apparatus presented in Figure 1 was used to measure heat generation and heat dissipation from LIB A and LIB B.

A total of 15 k-type thermocouples (TCs) were used, three on each side of the cell (in pairs), one in each clamp, three in each busbar and one to monitor the ambient as shown in Figure 1. For LIB A, all TCs were positioned along the width-centreline. Lengthwise, they were 5 mm from either end of the electrode-stack (TC1 and TC4 at the negative end, TC3 and TC6 at the positive end) and 45 mm from the negative end (TC2 and TC5). For LIB B, two pairs were positioned 5mm in (length and width-ways) from the corners on the cell edge opposite the tabs (TC1 and TC4, and TC2 and TC5). The final pair (TC3 and TC6) was positioned centrally between the tabs, 5 mm in from the edge of the electrode-stack.

All TCs were held using 3M TC2810 thermal epoxy. For the busbar and clamp, TCs were secured 6mm into the brass to ensure the most accurate reading. Temperature measurements were recorded by two TC-108 Pico dataloggers (manufactured by Pico Technology). The body of the apparatus was made from Celotex CW4000 solid insulation, thoroughly insulating the cells' surfaces. The cell, busbars and clamps fitted into specifically machined internal pockets in the insulation. A second block of insulation, shown in Figure 1 side view, sits on top of the lower half thus fully enclosing the cell. The busbars and clamps were fabricated from brass (CZ121), which has a specific heat capacity, $c_{p\,BB}$, of 0.380 kJ.kg^{-1}.K^{-1} and thermal conductivity, k_{BB}, of 123 W.m^{-1}K^{-1}.

All experiments were performed with the rig placed in a thermal chamber. Grooves were cut for all the TCs leading out of the insulation. The cell and both clamps were therefore thoroughly insulated, allowing neglection of convective heat transfer into the ambient of the thermal chamber. The busbars were also insulated, save their controlled-ends, which were entirely covered by Peltier elements (European Thermoelectric, APH-127-10-20-S) (PEs), one adhered to each.

The PEs were used to finely control the temperature of the non-cell-end of each busbar (hence forth referred to as the controlled-end). The PEs defined the boundary temperature within a purely conductive system, and therefore eliminated convection as a heat transfer mode from the system entirely. Using the PEs as the heat sink from the system reinforces the notion of the CCC as a purely conductive system parameter. The PEs were controlled using PID software embedded on an Arduino Uno with a motor controller shield (Cytron, RB-Cyt-116) and thermocouple reader (Lysignal BL-012), accurate to the nearest 0.25°C. The opposing side of the PE was cooled using a heat sink and fan.

Heat rejection from the cell tabs was monitored down the busbars shown in Figure 1. The busbars created a dominant path for heat

Table II. The layer component geometric and thermal properties for LIB A[15] and LIB B[55].

| Component	Negative CC	Positive CC	Separator	Anode	Cathode	Casing
LIB A: Calculated in-layer k_{eff}: 67.08 W.m^{-1}K^{-1}						
k/W.m^{-1}K^{-1}	398	238	0.34	1.58	1.04	238
Thickness per layer/mm	0.0210	0.0210	0.0240	0.0380	0.0290	0.1600
Number of layers	50	51	104	100	100	2
Volumetric proportion of cell	9.38%	9.38%	21.42%	33.93%	25.89%	2.75%
LIB B: Calculated in-layer k_{eff}: 38.75 W.m^{-1}K^{-1}						
k/W.m^{-1}K^{-1}	398	238	0.33	1.045	0.44	238
Thickness per layer/mm	0.0147	0.0151	0.0190	0.0737	0.0545	0.1600
Number of layers	24	25	54	50	50	2
Volumetric proportion of cell	4.53%	4.66%	11.72%	45.46%	33.62%	3.77%
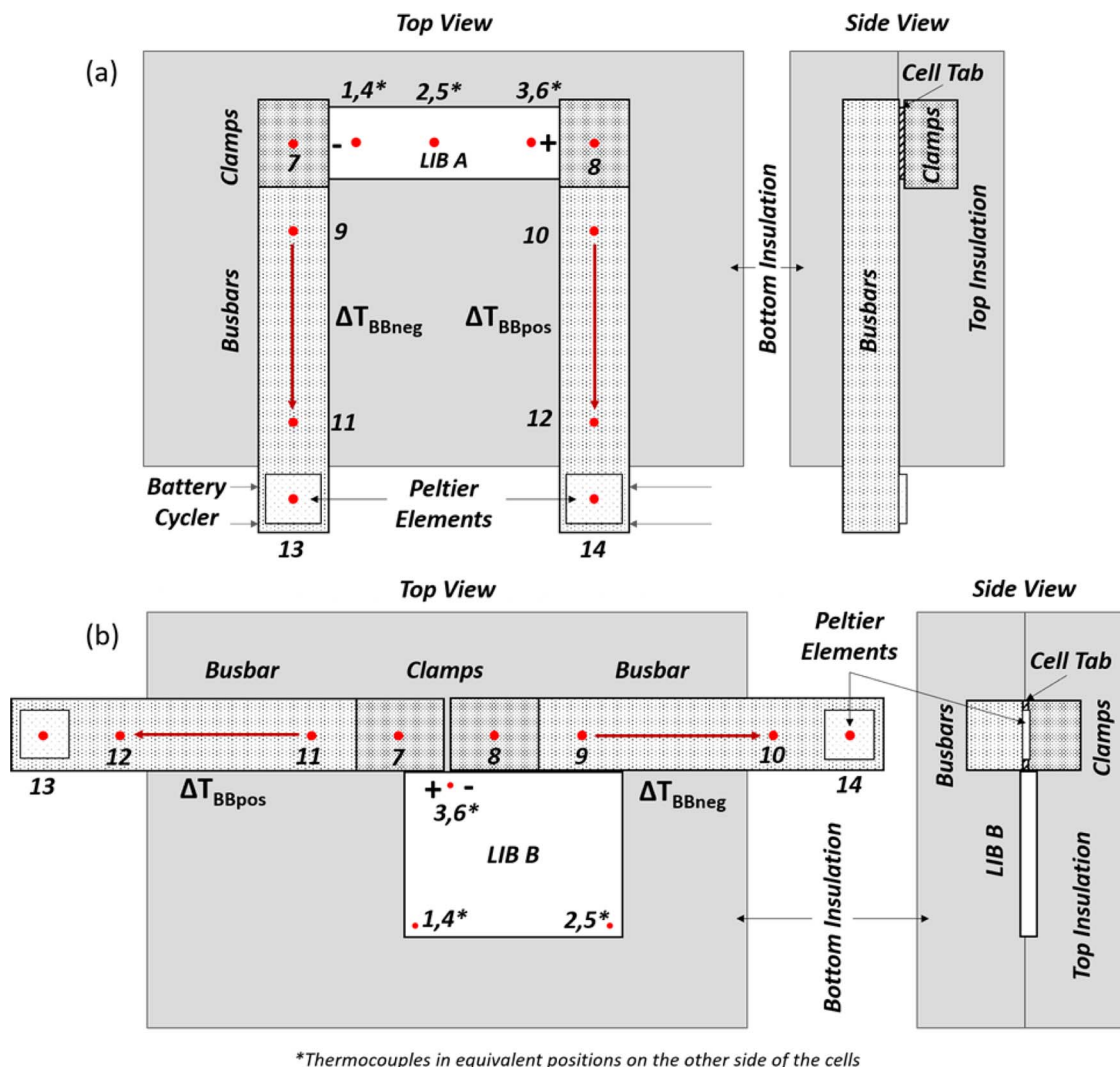
Figure 1. A schematic of the experimental apparatus used in the present investigation for each test, and thermocouple positions (numbered points) on (a) LIB A and (b) on LIB B.

rejection from the cell, therefore replicating a tab cooling scenario. It was essential that the derived CCCs were a function solely of the cell properties. Therefore, the busbars allowed for the full surface of the tabs to be clamped. The effect of the busbar properties on the CCC derivation were eliminated by ensuring the tab temperature (necessary for CCC calculation) was measured very close to the tab, in the tab clamps, TC7 and TC8 for the negative and positive tab temperatures respectively. Therefore, the thermal gradient built up in the busbar, used to monitor rate of heat rejection, would not affect tab temperature. In this manner, the same CCCs may be calculated for the tested cells using geometrically of thermally dissimilar busbars in a different experimental rig.

The busbars were sufficiently long to ensure 1D conductive heat transfer from TC9 to TC11, and correspondingly from TC10 to TC12, a distance of 100mm as outlined by the respective arrows and defined as x_{BB}. The rate of heat transfer through the negative busbar, $\dot{Q}_{neg}$, calculated using Equation 3, where A_{BB} is the cross-sectional area of the bar and ΔT_{BBneg} is the difference between TC9 and TC11. The same equation is used for $\dot{Q}_{pos,}$ using ΔT_{BBpos}. The lengthened bars alter the transient response of the system: increasing the thermal mass and lag of the system. However, when the cell is in a thermal steady state, i.e. heat is generated at the same rate it is rejected, the system is unaffected by the extended busbars. Unrecorded conductive heat loss down the cables was highlighted in the literature[56] as a possible source of error in similar experimental procedures. The error was eliminated

with this experimental apparatus, as conductive heat transfer rate was determined on the cell side of the cables. The cross-sectional area of the busbar was large enough so that ohmic heating in the busbar was a negligible error, calculated to be 0.0169W when a current of 20A was being passed. Brass was selected over copper as peak electrical conductivity was not necessary, due to the busbar cross-section. Brass has a comparatively low thermal conductivity, which allowed for a significant thermal gradient to build up between the upstream and downstream TCs, and thus reduce the error in the thermal gradient measurement. The busbars were cleaned and polished at the point of contact with the tab to ensure minimal electrical contact resistance, and consequent ohmic heating.

$$\dot{Q}_{neg} = \frac{k_{BB}}{x_{BB}} A_{BB} \Delta T_{BBneg} \qquad [3]$$

To ensure even pressure and contact over the entire cell tab, tab temperatures were measured via the clamps, preventing the need for a thermocouple between the clamp and tab. Thermal paste (Fischer Elektronik, WLPK 10) was applied between the top side of the tab and clamp to ensure a minimal thermal gradient across the interface. Additionally, each cell was held in place with the clamps and busbar as close to the edge of the tab as possible, to minimize the length of exposed tab through which heat must dissipate. This was identified as a critical part of the procedure to ensure repeatability of the experiment, since an additional length of exposed tab would have resulted in a larger
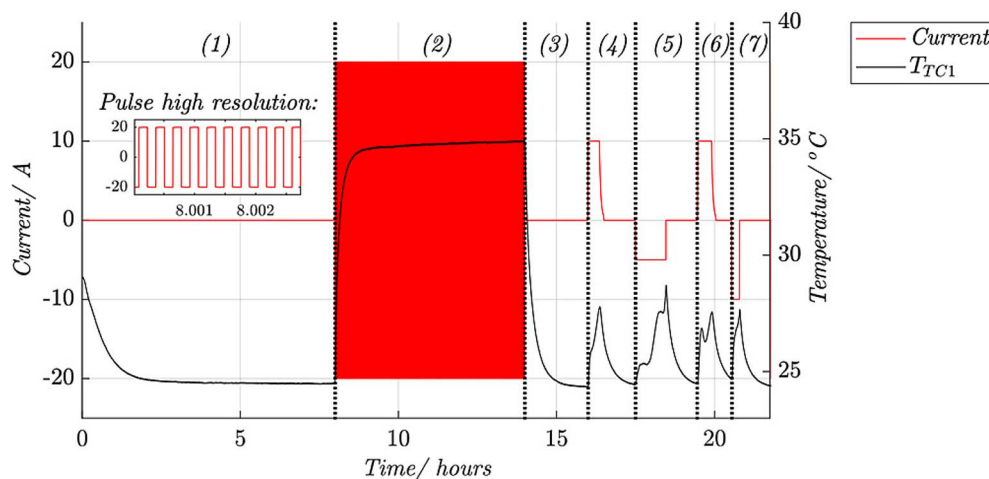
Figure 2. Current profile for the defined test procedure and the temperature recorded by TC1 during Test 1.

measured temperature difference from the cell to the tab and alter the result.

Procedure.—The cells were cycled with a Bio logic BCS-815 battery cycler. The full cycle procedure is listed below, and the current profile and cell thermal response is displayed in Figure 2. The first 10 seconds of the pulsing cycle is shown with a higher resolution, in the upper left of the figure. The TCs were calibrated, by removing any offsets, in the final hour of Step 1, where thermal equilibrium within the chamber was assumed. The SOC was roughly set prior to the pulsing period of each test. The exact SOC for each test was determined from the cell's OCV prior in the final hour of Step 1. The busbar temperature was then held at the set temperature by using PEs at the start of Step 2, thus ensuring TC calibration was unaffected.

The square wave pulsing method was used in order to maintain the SOC relatively constant within the cell over an extended period of time, whilst current was consistently being passed and therefore heat was being generated at a steady rate. The rapid switching time of the cell cycler, 1ms, was essential for this. The heat generated during this procedure is mainly irreversible heat (first term in Equation 1) resulting from the charge transfer overpotential at the interface and ohmic heat. The concentration gradients are not significantly influenced due to the very small number of ions that are rocked back and forth in the electrolyte between the two electrodes.[57] As the SOC is changed by a small amount within one period, the reversible entropic heat can be ignored, but can sometimes be seen in small oscillations.[58] The necessity of the pulsing method is examined in detail at the end of this section. A 1C discharge test (Step 5) was performed at end of each pulsing test to check if there is noticeable degradation. In addition to capacity check, temperature change during the discharge was also compared. To reset the cell to the desired SOC the cell was charged back to 100% (Step 6), then 1C discharged till the desired number of coulombs had been passed.

1. 8-hour rest to ensure thermal equilibrium across all apparatus within the thermal chamber
2. Square wave current pulsing for 6 hours at various C-rates at 1 Hz
3. 2-hour rest to reach consistent thermal conditions prior to degradation analysis
4. 1C CC-CV Charge to 4.2V with a 500mA cutoff, followed by 1-hour rest
5. 1C CC discharge to 2.7V for degradation analysis, followed by 1-hour rest
6. 1C CC-CV charge to 4.2V with 500mA cutoff, followed by 0.5-hour rest
7. 1C discharge to desired cell SOC, followed by a 2-hour rest

Apparatus Characterization

Due to imperfect thermal insulation, the apparatus was characterised to quantify unavoidable losses. The measured data was calibrated based on the following results. The apparatus was characterised by introducing a known amount of heat into both cell types, in order to determine the fraction of the heat that was rejected through the tabs, and the fraction lost into the insulation. A resistive heater (RS Pro), set to generate 1.49W of heat, was adhered centrally to the top surface of LIB A1 and B1. For LIB A, calculated busbar heat transfer rate amounted to 1.24W (83.2% of the inputted heat rate), when the cell was in thermal equilibrium. Thus 16.8% of the heat was lost to other, unmeasured, thermal dissipation pathways: conduction through the solid insulation and TC wires. The thorough insulation of the cell leads to a working conclusion that the rate of convection from the cell to the ambient is negligible. For LIB B, just 0.73W (49.0% of the inputted heat rate) was measured conducting along the busbars, in steady thermal conditions. The rise in heat losses was expected, given LIB B's larger surface area and smaller tabs. The analysis in this study is based around the heat dissipated through the tabs, so these losses were not detrimental to the investigation, so long as they are accounted for. A rate of heat loss, $\dot{Q}_{loss}$, in proportion with the rate of conductive heat transfer through the busbars, $\dot{Q}_{trans}$, can therefore be defined through Equation 4. The coefficient of proportion, α_{loss}, is dependent on the cell type: 0.1975 for LIB A and 1.0411 for LIB B.

$$\dot{Q}_{loss} = \alpha_{loss} \dot{Q}_{trans} \qquad [4]$$

Pulsing Period Justification

During the pulsing period, the electrode potentials and reaction currents are virtually constant. The pulses lead to instantaneous ion migration in the electrolyte. The heat is therefore generated throughout the cell, due to the movement of ions in the electrolyte.[57] A resistive heater, whilst effective for apparatus characterization, was not able to replicate the thermal conditions within the cell under load. A comparison between internal cell heat generation through current pulsing, and external surface heating through the resistive heater was numerically conducted.

In this work, a two-dimensional electro-thermal model developed previously,[16] was used. The model was developed in MATLAB R2017a using Simulink (v8.8) and Simscape toolbox (v4.1). The model was parametrised for LIB A. The model was specifically developed to account for non-electrode-stack components such as the tab weld to ensure an accurate internal temperature prediction. For this work, there were no changes made to the core cell model structure and the cell parameters. The thermal boundary condition was changed to reflect the experimental setup used in this work. A thermally insulating condition was applied to the cell electrode-stack
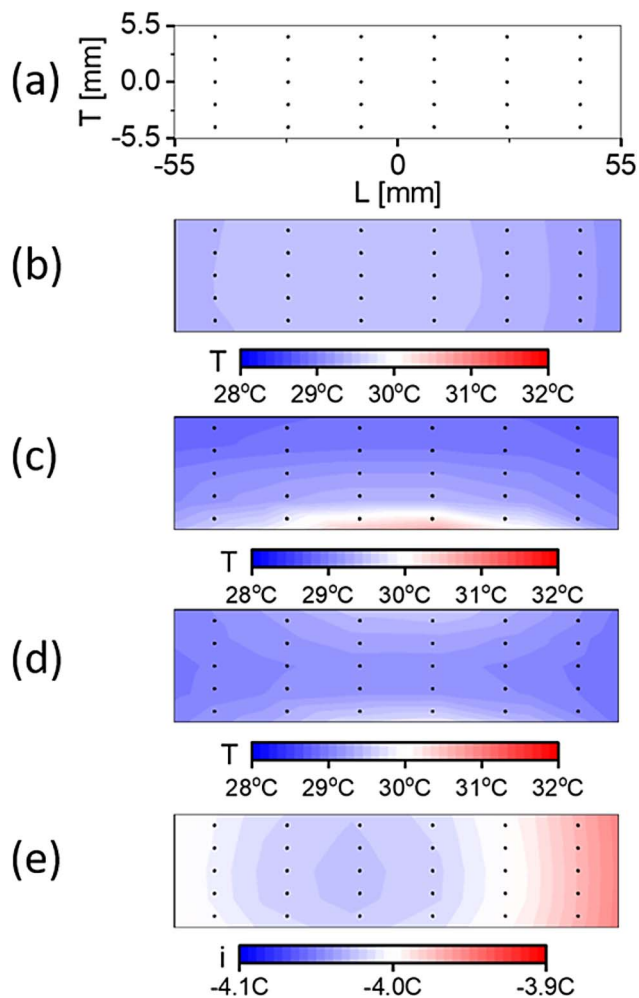
Figure 3. Temperature distribution profiles produced in the defined ECM, modelling LIB A under different heat loads. All with 50% SOC and 25°C ambient temperature. (a) Model geometry; (b) 20A pulsing cycle; (c) 1.49W of heat added uniformly across one surface of the modelled cell; (d) 1.49W of heat added uniformly across both surfaces of the modelled cell; (e) current density distribution profile during 20A pulsing cycle.

surfaces. At the cell tabs, the brass busbars as well as the PE controlled heat sinks were modelled.

Total equivalent thermal resistance at the surface and the tab of the unit cell is given by Equations 5 and 6 respectably.

$$R_{total,surf} = R^*_{boundary} + R^*_{insulation} + R_{interface} + R_{casing} \qquad [5]$$

$$R_{total,tab} = R^*_{boundary} + R^*_{insulation} + R_{interface} + R_{BB} + R_{tab} \qquad [6]$$

$R_{total,surf}$ is the total thermal resistance at the surface and $R_{total,tab}$ is the total thermal resistance at the tab, $R^*_{boundary}$ is the equivalent thermal resistance associated with heat flow from the conductive system boundary, $R^*_{insulation}$, is the equivalent thermal resistance of the insulation material, $R_{interface}$ is the equivalent thermal resistance associated with the thermal interface material, R_{casing} is the equivalent thermal resistance associated with of the cell casing, R_{BB} is the equivalent thermal resistance associated with the brass busbar and R_{tab} is the equivalent thermal resistance associated with the weld point at each tab.

The induced thermal conditions from pulsing at 1 Hz, with a current magnitude 20A and a cell SOC of 50%, are shown in Figure 3b. The internal temperature distribution, from surface (resistive) heating to the cell's top surface at the same heat rate (1.49W) is shown in Figure 3c. The maximum cell temperature difference in the former is less than 1°C, whilst in the latter it is greater than 3°C. The

Table III. Thermal properties of key components.

Component	Mass (kg)	Thermal Conductivity (W.m^{-1}K^{-1})	Specific Heat Capacity (kJ.kg^{-1}.K^{-1})
LIB A	0.123	n/a	1.030
LIB B	0.165	n/a	1.008
Busbar	0.601	123	0.380
Clamp	0.110		
Insulation	n/a	0.023	n/a

pulsing experiment induces a thermal gradient within the electrode plane, while the surface resistive heating induces a through thickness thermal gradient. Differences in the direction and the magnitude of the thermal gradient could lead to altered thermal pathways and result in dissimilar transfer from the tabs. Figure 3d shows the temperature distribution induced by resistive heating on both sides, with the same total heat input. The magnitude of the thermal gradients across the cell is reduced, compared to the single side heating, but the direction of the gradient is still not representative of operation. Further to this, the difficulty with measuring any reliable cell temperature would be heightened, should both top and bottom surfaces be covered by resistive heaters.

The model indicates that the developed pulsing cycle ensures a more uniform heat generation distribution from all regions of the cell. Figure 3e displays the current density across the cell when the pulsing cycle parameters are inputted into the model. The results are consistent with previous studies[15,16] analysing current distribution within an operating cell, being cooled at the tabs. Therefore, it is seen as the most effective method to input a constant and uniform rate of heat. Figure 3e also highlights the site at which the peak cell temperature is found in the presented model: central on the cells' width and 45mm from the negative end. This geometric position was used to position TC2 and TC5 in the experimental apparatus.

The mass of a single cell, busbar and clamp were determined using a technical balance. The specific heat capacity of LIB A, $c_{p\,LIB\,A}$, was empirically measured through a calorimetry experiment conducted in an accelerating rate calorimeter ($ARC\,EV+$) manufactured by Thermal Hazard Technology. These properties are collated in Table III.

The cell average temperature, $T_{cell,av}$, is calculated assuming a constant thermal gradient from the point at which the maximum temperature, $T_{cell,max}$, is observed to the respective tabs. Equation 7 defines $T_{cell,av}$ for LIB A, and Equation 8 for LIB B. In each case, the equation coefficients are calculated based on the specific cell geometry and exact TC placement. The busbar average temperatures, $T_{BBneg,av}$ and $T_{BBpos,av}$ are calculated at their centre of mass, thus assuming constant thermal gradients along their length, according to Equation 9 (and similar for the positive busbar). T_{neg} and T_{pos}, which are recorded by TC7 and TC8 respectively, are additionally used for the clamp temperatures, $T_{clamp,neg}$ and $T_{clamp,pos}$.

$$T_{LIB\,A,av} = \frac{9}{22}\left(\left(\frac{T_{TC1} + T_{TC4}}{2}\right) + \left(\frac{T_{TC2} + T_{TC5}}{2}\right)\right)$$
$$+ \frac{13}{22}\left(\left(\frac{T_{TC2} + T_{TC5}}{2}\right) + \left(\frac{T_{TC3} + T_{TC6}}{2}\right)\right) \qquad [7]$$

$$T_{LIB\,B,av} = \frac{19}{58}\left(\left(\frac{T_{TC1} + T_{TC4}}{2}\right) + \left(\frac{T_{TC3} + T_{TC6}}{2}\right)\right)$$
$$+ \frac{39}{58}\left(\left(\frac{T_{TC2} + T_{TC5}}{2}\right) + \left(\frac{T_{TC3} + T_{TC6}}{2}\right)\right) \qquad [8]$$

$$T_{BBneg,av} = \frac{T_{TC9} + T_{TC11}}{2} \qquad [9]$$

Table IV. Summary of all tests in the present investigation. Cell average temperature is determined as the mean temperature of the cell, over the entirety of the steady-state region. All tests are conducted with an ambient air temperature of 25°C, with the exception of Test 5 (10°C).

Cell Name	Test Number	SOC/%	Current/A	Cell Average Temperature/°C	CCC_{tot}/W.K^{-1}
LIB A1	1	24.28	20	33.83	0.336
LIB A1	2	51.94	20	30.79	0.341
LIB A1	3	51.95	20	30.70	0.339
LIB A1	4	51.99	15	28.44	0.339
LIB A1*	5	53.60	20	19.89	0.339
LIB A1	6	49.68	7.5	25.56	0.328
LIB A1	7	51.99	15	28.10	0.333
LIB A2	8	52.09	20	30.75	0.324
LIB A2	9	50.07	20	31.07	0.325
LIB A2	10	44.76	15	29.04	0.328
LIB A3	11	25.13	20	34.25	0.327
LIB A3	12	51.97	20	31.09	0.330
LIB A3	13	51.98	20	30.98	0.330
LIB A3	14	51.92	15	28.86	0.336
LIB B1	15	14.59	15	29.74	0.196
LIB B1	16	53.35	15	27.59	0.208
LIB B1	17	53.32	15	27.57	0.209
LIB B1	18	50.42	16	28.51	0.211

Test Conditions

The experimental procedure was repeated for 18 tests. Three LIB As and one LIB B were used in experimentation: from here referred to as LIB A1, A2, A3 and B1. Procedural parameters, current magnitude, busbar controlled-end temperature and cell SOC, were varied to evaluate heat dissipation from the cells under differing operational conditions. Table IV summarises each test. The different rates of cell heat generation, coupled with the range of busbar controlled-end temperatures used, allowed variance of the cell temperature during the pulsing cycle. For all tests on LIB A, elevated steady-state cell temperature therefore ranged from 19.89°C (Test 5) to 34.25°C (Test 11). The calculated CCC$_{tot}$ are also displayed, for clarity, and will be referred to in analysis.

A check was conducted following each test, to ensure no noticeable degradation had occurred within the cells. Results from the analysis on Tests 1–4 are evaluated here. The aim of this analysis is to ensure the heat generation and heat rejection pathways within the cell are not affected by the induced pulsing cycle.

Figure 4 shows the voltage curves over the 1C discharge, and the resulting change to $T_{cell,max}$. The discharged capacity was calculated to be 95.83%, 95.83%, 95.90% and 95.76% of the total cell capacity, for Tests 1–4 respectively. Quantitatively, it was measured to be 3.57°C, 3.53°C, 3.48°C and 3.46°C for Test 1–4 respectively. The maximum-to-minimum deviation in this dataset is just 3.18%, and this is attributed to TC measurement error and inconsistent experimental boundary conditions.

Results

Cell thermal behavior.—Figure 5 displays the determined instantaneous heat rates within the system during Test 1, which is used as the example in the following section. The heat rate components may be split into two categories: heat generation rates and heat rejection rates. The cell temperature rises gradually during the initial transient region. Here, a significant proportion of the total heat generated remains in the system, causing temperature rise in the cell and busbar assemblies. These portions of the heat rate, $\dot{Q}_{cell,gain}$ and $\dot{Q}_{BB,gain}$ respectively, are determined through Equations 10 and 11.

$$\dot{Q}_{cell,gain} = m_{cell}c_{p,cell}\frac{dT_{cell,av}}{dt} \qquad [10]$$
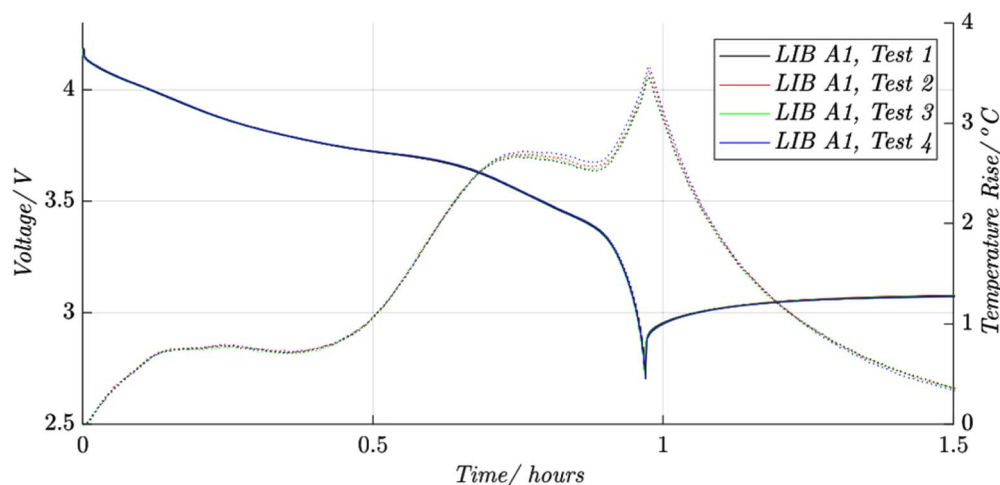

Figure 4. Recorded cell voltage (solid line) and temperature rise (dashed line) over the course of a 1C discharge, following Tests 1–4.
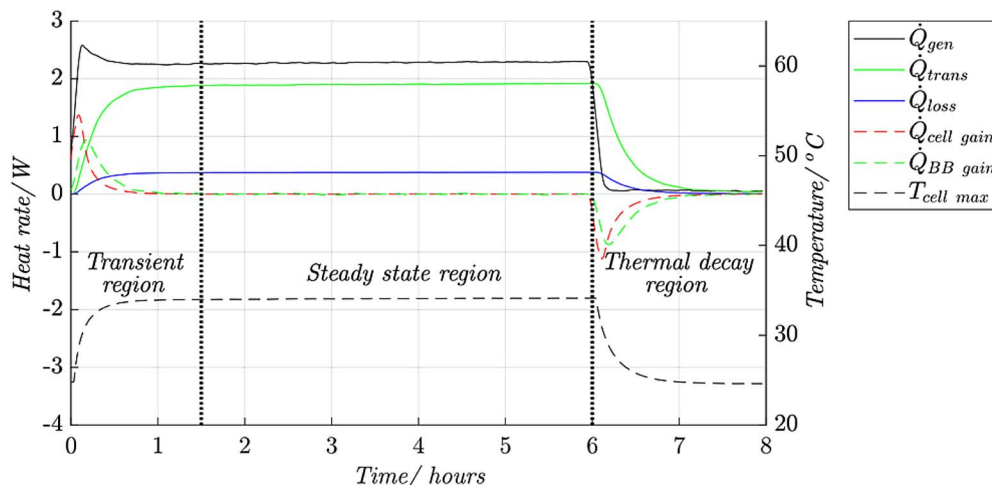
Figure 5. Cell heat rates and cell temperature over the pulsing cycle.

$$\dot{Q}_{BB,gain} = m_{BB}c_{p\,BB}\left(\frac{dT_{BBneg,av}}{dt} + \frac{dT_{BBpos,av}}{dt}\right)$$

$$+ m_{clamp}c_{p\,BB}\left(\frac{dT_{neg}}{dt} + \frac{dT_{pos}}{dt}\right) \qquad [11]$$

The increasing temperature difference from the cell to the busbar cooled ends induces a rising rate of conductive heat transfer through the cell tabs. $\dot{Q}_{neg}$ and $\dot{Q}_{pos}$ are derived from the thermal gradients along the busbars, as set out in Equation 3 and their sum is plotted as $\dot{Q}_{trans}$. The rate of heat rejection through the cell surfaces, rather than through the cell tabs, $\dot{Q}_{loss}$, is defined in Equation 4. The heat rate components are summed to give $\dot{Q}_{gen}$, the experimentally derived cell heat generation rate, Equation 12. Steady thermal conditions are achieved when $\dot{Q}_{trans} + \dot{Q}_{loss} = \dot{Q}_{gen}$, and therefore $\dot{Q}_{cell,gain}$ and $\dot{Q}_{BB,gain}$ are negligible. $\dot{Q}_{gen}$ reduces as T_{cell} rises. This phenomenon, displayed in the transient period of Figure 5, acts constructively with the thermal system's described energy balance to accelerate the rate at which steady state conditions are achieved.

$$\dot{Q}_{gen} = \dot{Q}_{cell,gain} + \dot{Q}_{BB,gain} + \dot{Q}_{trans} + \dot{Q}_{loss} \qquad [12]$$

Temperature differences, from cell to tab, which drive the conductive heat transfer must be considered for a quantitative comparison.

Equations 13, 14 and 15 define ΔT_{neg}, ΔT_{pos} and ΔT_{av}, respectively.

$$\Delta T_{neg} = T_{cell\,max} - T_{neg} \qquad [13]$$

$$\Delta T_{pos} = T_{cell\,max} - T_{pos} \qquad [14]$$

$$\Delta T_{av} = T_{cell\,max} - \frac{T_{neg} + T_{pos}}{2} \qquad [15]$$

Figure 6 displays the components of $\dot{Q}_{trans}$. The results show that the negative tab provides a more thermally conductive pathway. The ratio $\dot{Q}_{pos}/\dot{Q}_{neg}$, for each of the 14 tests conducted on LIB A, is shown in Figure 7. The mean averages for the duration of the steady temperature region were used to calculate the ratio. Results are consistent: the standard deviation in the results for LIB A1, A2 and A3 are 0.0111, 0.0101 and 0.0026 respectively, whilst the overall standard deviation is 0.0106. Also included is the ratio for the control test, which is 12.8% below the set's mean. The discontinuity between results from pulsing tests and results from the resistive heater control further validate the necessity to use internal cell electrochemical reactions to add heat to the system, in a manner representative of application.

The $\dot{Q}_{pos}/\dot{Q}_{neg}$ ratio was also determined from the outputted model data when the same pulsing cycle was inputted, and two specific cases are included in Figure 7. The inputted current magnitude was 20A, the cell SOC was 50% and the busbar controlled-end temperature was varied from 10°C to 25°C. The ambient temperature of the chamber,
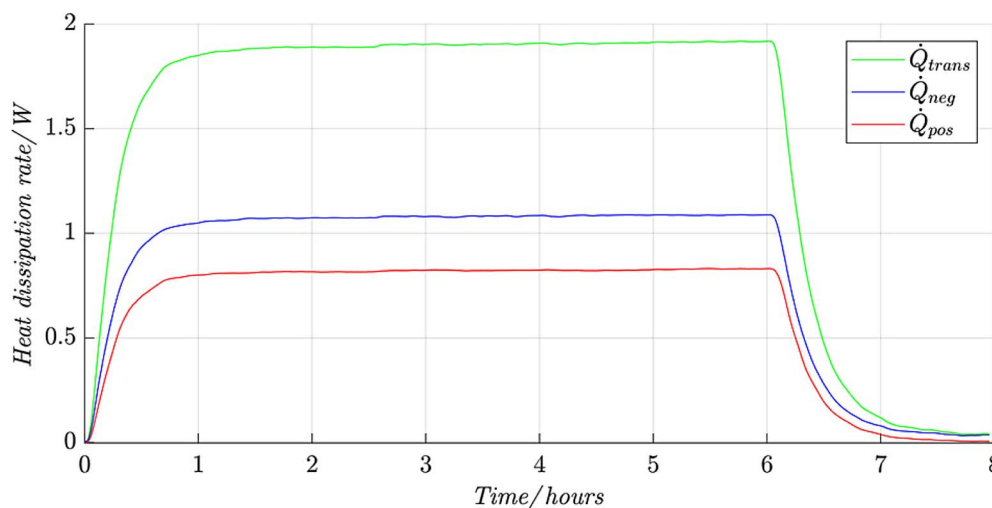

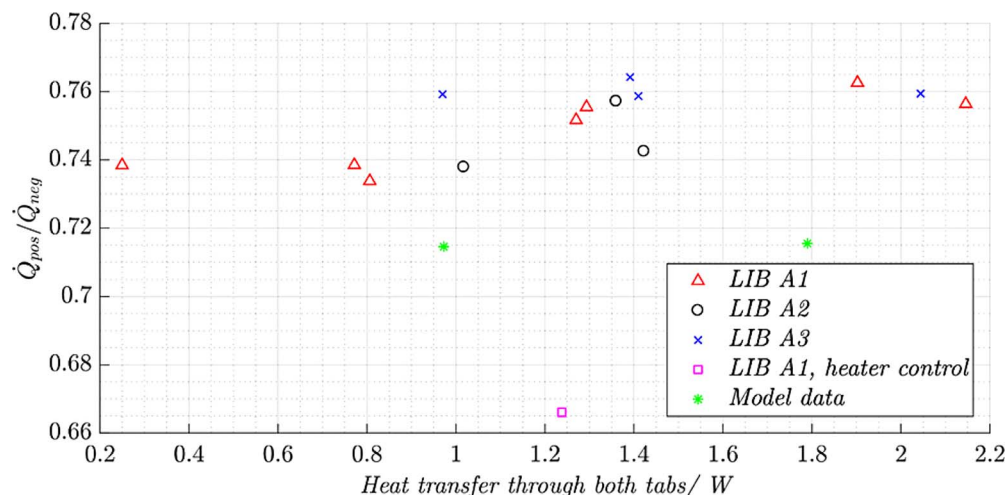**Figure 6.** The heat transfer rates through the tabs over pulsing cycle.

Figure 7. The positive: negative tab heat transfer rate ratio for each of the 14 tests conducted on LIB A.

which affected the minor loss of heat through the insulation, was varied to match the busbar controlled-end temperatures. It is apparent that the model exhibits similar thermal pathway characteristics: the mean modelled ratio is 5.0% below the mean of the experimental data.

Figure 8 shows the temperature differences, ΔT_{neg}, ΔT_{pos} and ΔT_{av}, for the duration of the pulsing period. The negative tab's higher steady state temperature can be attributed to it being more thermally conductive than the positive tab, and therefore able to more closely match the temperature of the cell. This characteristic may also be observed in the transient thermal response of each tab during the initial stage of the pulsing period. From the onset of pulsing, in Test 1, the negative tab takes 594s to reach 95% of its temperature in the steady state region. The positive tab's response is 882s, a time increase of 48.5%. Response time difference is also evident in the thermal decay region. Applying the same definition of thermal equilibrium, the positive tab's response is 39.8% slower than the negative tab.

Discussion

Cell cooling coefficient.—The quality of thermal pathway through each tab can only be quantified by considering the introduced thermal performance measures: rate of heat transfer and cell to tab temperature difference, with respect to one another. This is because they are coupled, and therefore variance of either one has a direct effect on the other. The cell cooling coefficient facilitates this. Analysis will show the CCC to be independent of all other procedural characteristics: current magnitude, cell SOC and cell operating temperature. The CCCs are therefore constant values for a given cell, dependent only on its unique geometric and constituent material and interface thermal properties.

Equations 16, 17 and 18 define CCC_{neg}, CCC_{pos} and CCC_{tot}, values for quantitatively evaluating the quality of the thermal pathways used for heat dissipation through either or both cell tabs. Dimensionally watts per degree Kelvin, the coefficients describe the rate of conductive heat transfer induced by a certain temperature drop. Figure 9 displays CCC_{neg}, CCC_{pos} and CCC_{tot}, calculated over the course of Test 1's steady state region. The CCCs are true values only in the steady temperature region as they rely upon the assumption that heat is dissipating from the cell at the same rate it is generated. The previously discussed enhanced negative tab pathway is observable through the higher CCC_{neg} value, compared to CCC_{pos}.

$$CCC_{neg} = \frac{\dot{Q}_{neg}}{\Delta T_{neg}} \qquad [16]$$

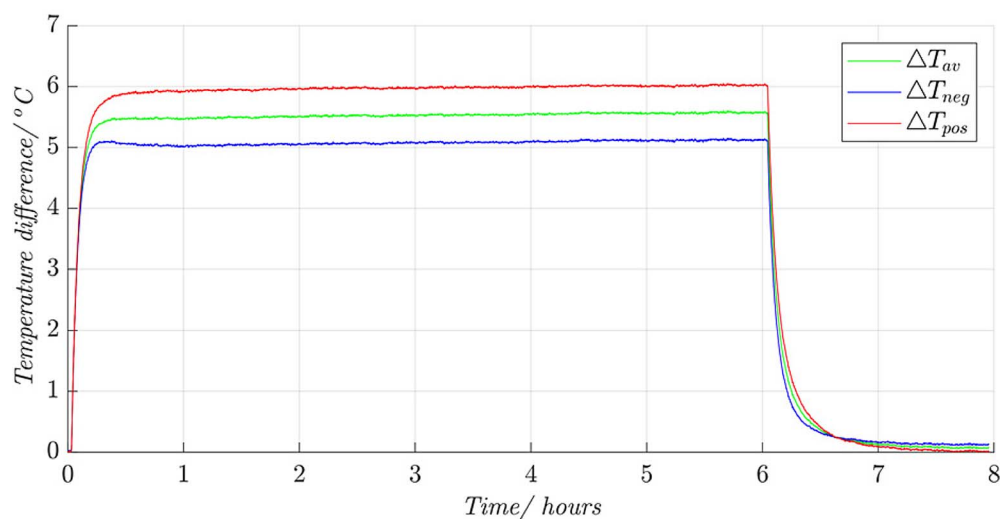$$CCC_{pos} = \frac{\dot{Q}_{pos}}{\Delta T_{pos}} \qquad [17]$$

Figure 8. Temperature differences, from the cell maximum temperature to the tab temperatures, over the pulsing cycle.
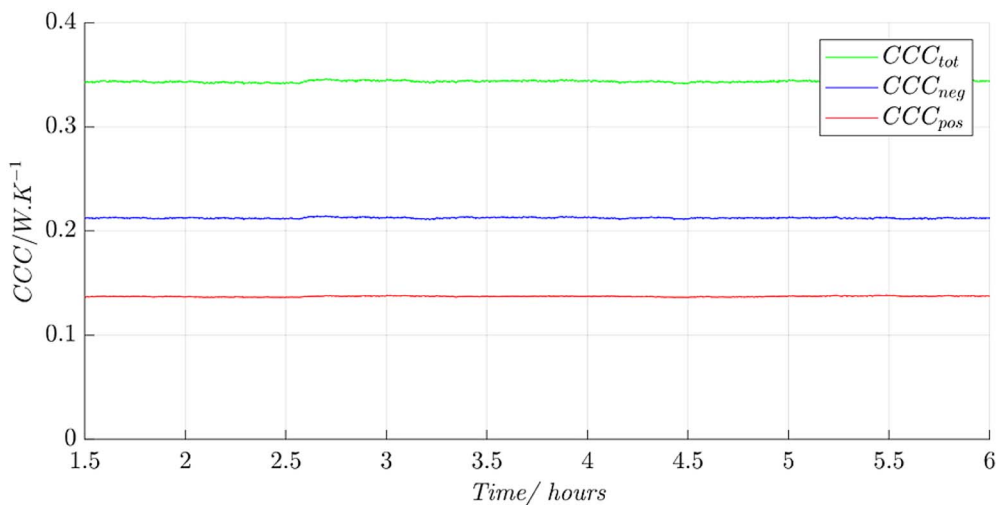
Figure 9. The cell cooling coefficients calculated for LIB A1, from results in Test 1, for the entirety of the steady state region within pulsing cycle.

$$CCC_{tot} = \frac{\dot{Q}_{trans}}{\Delta T_{av}} \qquad [18]$$

The CCC is thus a single measure defining an individual cell's ability to dissipate heat through a certain pathway. Therefore, the mean CCC values, averaged across the steady state region, are taken. Figure 10 displays the CCCs calculated from every test on LIB A1. The CCC is also a robust cell parameter, ascertainable under any operational conditions that achieve steady state cell temperatures, elevated above the busbar controlled-end temperature and thus inducing heat transfer. Maximum and standard deviation error analysis, summarised on the top row of Table V, was conducted on the derived CCCs from each

test on LIB A1. The results find the methodology for deriving the CCCs to be repeatable for a given cell. The high levels of correlation are achieved under the experimental parameter variance detailed in Table IV.

Figure 11 shows CCC_{neg}, CCC_{pos} and CCC_{tot}, for each test carried out. The middle row of Table V summarises the error analysis conducted on all 14 tests carried out with LIB A. The dataset standard deviations remain low, suggesting CCC values are constant for a certain cell model. The maximum deviation from the datasets' mean values increase. Normal distribution theory states that the value range of dataset increases with its size, and therefore the additional variance was expected.

Variance in calculated CCC values may also be attributed to experimental error and cell manufacture variation, which are coupled to an extent. Figure 12 presents images of the negative and positive tabs on LIB A1, A2 and A3. Annotation 1 highlights the inconsistent and unsmoothed surface left at the weld site for the positive tabs. These inconsistencies could lead to variation in both thermal and electrical contact resistances. Annotation 2 highlights the inconsistent position of the positive tab, relative to the tab: for the three cells used, this was found to vary from 0.4 mm left of centre to 0.3 mm right of centre: a deviation of 3.5% across a 20 mm tab width which would be an error carried into the cross-sectional area of that portion of the thermal pathway. Annotation 3 highlights the misaligned angle of the positive tab

Table V. Error analysis for the cell cooling coefficient derivation process.

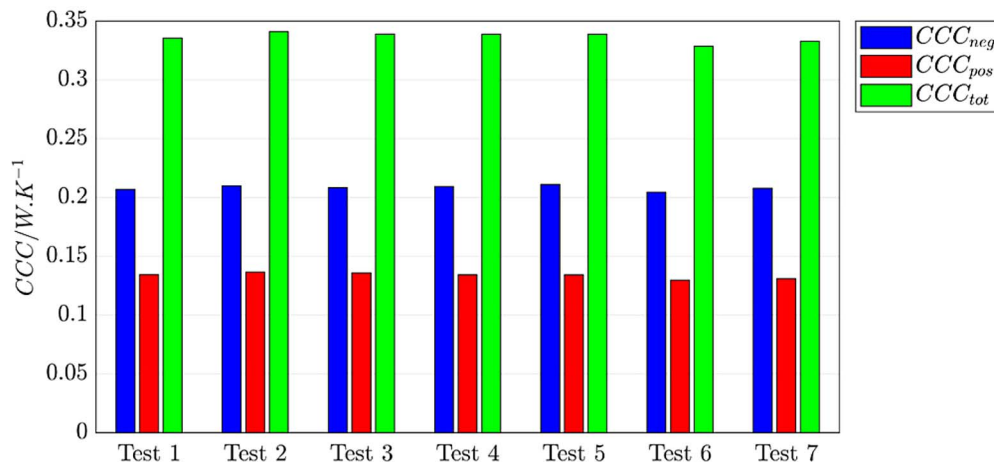|	Maximum deviation from dataset mean			Dataset standard deviation		
	CCC_{neg}	CCC_{pos}	CCC_{tot}	CCC_{neg}	CCC_{pos}	CCC_{tot}
LIB A1 tests	1.81%	3.04%	2.33%	0.0044	0.0033	0.0075
All LIB A tests	4.74%	5.53%	2.63%	0.0047	0.005	0.0057
LIB B1 tests	4.40%	5.97%	4.98%	0.0038	0.0033	0.0069

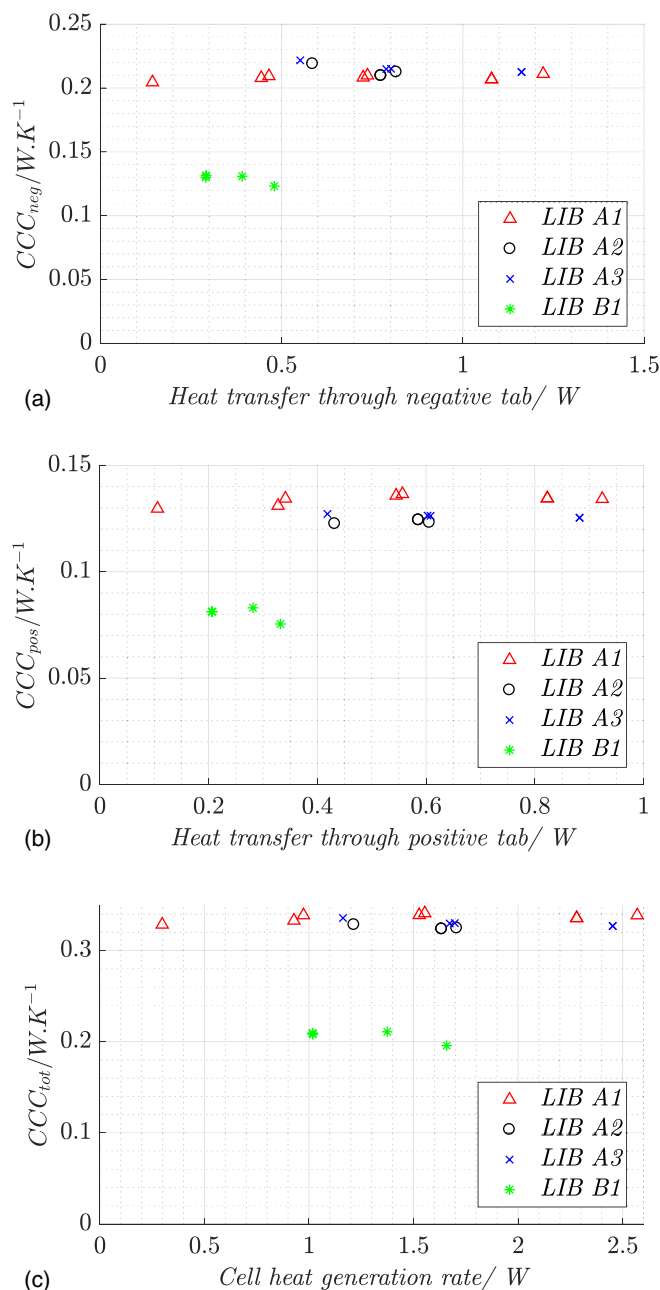**Figure 10.** The cell cooling coefficients for each test carried out on LIB A1.

Figure 11. The cell cooling coefficients for all tests. (a) Negative tab: CCC_{neg}; (a) Positive tab: CCC_{pos}; (c) Combined: CCC_{tot}.

Figure 12. The negative and positive tabs of each LIB A used in experimentation. Annotation highlighting manufacture variation.

CCC_{tot} values. This is regardless of the process via which the elevated cell temperature is altered: be it busbar controlled-end temperature change, current magnitude variation or cell SOC adjustment. The thermal and geometric properties of the individual materials within the cell electrode-stack are themselves dependent on temperature, and therefore slight variation of the true CCC values for the cell were expected, to a very small degree. The resolution and accuracy provided by the TCs in the present investigation were unable to associate a correlation between cell temperature and experimentally derived CCCs.

The independence of current magnitude and SOC variance on the CCC derivation is graphically displayed in Figure 11. The CCCs for each test are plotted against the steady state $\dot{Q}_{gen}$, which is dependent on current magnitude, cell temperature and SOC. A correlation between $\dot{Q}_{gen}$ and the CCCs is not observable.

Figure 11 also shows the CCCs for each test conducted on LIB B1. Error analysis is summarised in the bottom row of Table V. The CCC derivation process, based on the assumption of independence from factors inducing variation in $\dot{Q}_{gen}$, is shown to be functional for LIB B, despite the considerable geometric and material dissimilarities with LIB A. The CCC accounts for every parameter variation, be it a material thermal conductivity or a geometric dimension, detailed in Table I and Table II. The CCC also accounts for other physical properties, such as the thermal resistances caused by the welding of the electrical tabs and the current collectors, or the thermal conductivities of the electrode-stack materials in wetted state. The information is refined to a single value for each thermal pathway of interest, as summarised in Table VI.

The present shortfall in cell heat rejection understanding is evidenced by the complexity and coupled nature of the individual geometric and thermal parameters governing the process. Deriving a single empirical value is far more feasible than setting out to determine the coupling of each thermal conductivity and physical dimension of a cell. The output, i.e. a quantity defining heat rejection to a cooled surface of a cell, is the same. Therefore, the empirically determined CCCs can be of significant benefit for thermal characterization and subsequently for cell-to-cell comparison. From Table VI, it is

on LIB A3 (the same can be seen, labelled by 5, for LIB A2's negative tab). Consequently, the exposed length of tab on the cell side of the weld was inconsistent across the tab's width, reducing from 1.2 mm to 1.0 mm. This would have a direct effect on the cell to tab temperature difference for a given rate of heat rejection. Fabrication variation is also evident at the negative tab. Annotation 4 highlights the different amounts of resin leaked from the pouch. This meant a greater length of tab, directly affecting the thermal pathway quality, is exposed between the end of LIB A1's pouch material and the point at which the clamp could be applied: 0.6 mm for LIB A1, 0.4 mm for LIB A2 and 1.0 mm for LIB A3. Equivalent rates of heat transfer through the negative tab would have generated larger cell to tab temperature differences for LIB A1.

Table IV allows comparison of all LIB A tests. It can be seen that the cell's temperature, averaged over the course of the time period used for CCC calculation, has no observable effect on the derived
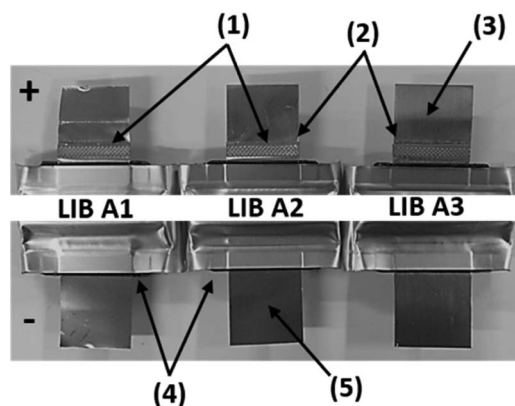
Table VI. All tab cell cooling coefficients for LIB A and LIB B.

	LIB A	LIB B	LIB A enhancement
CCC_{neg}	0.2117	0.1282	65.13%
CCC_{pos}	0.1294	0.0793	63.18%
CCC_{neg} enhancement	63.6%	61.7%	-
CCC_{tot}	0.3324	0.2043	62.70%

Table VII. Key performance metrics of LIB A and LIB B.

Cell	CCC_{tot}/W.K^{-1}	Max. continuous discharge rate/A.(Ah)$^{-1}$	Capacity/Ah
LIB A	0.3324	30	5
LIB B	0.2043	5	7.5

apparent that the negative tab, compared to the positive, provides a pathway 63.6% more capable of conducting heat from the cell for LIB A, and 61.7% more capable for LIB B. Focussing on cell-to-cell comparison, using CCC_{tot}, LIB A is 62.7% more able to dissipate a given quantity of heat through the tabs. These quantities, comparing two cells with similar form factors, can be used directly for application to improve designs of cell thermal management systems.

Thermal characterization.—The CCC defines conductive heat transfer due to an applied thermal gradient, and in this respect is comparable to established thermal coefficients: the Biot number, thermal conductance or thermal resistance. The CCC, however, defines heat rejection to a specific cooled surface of a cell, which itself is generating heat. This contrasts with the three identified thermal coefficients, which parameterise a body's ability to conduct heat from one plane to another. Attempting to derive the CCC in this manner, using external heat sources, has been analyzed and deemed unsuitable in this investigation.

Additionally, the CCC is an empirical and immediately applicable coefficient, as it defines heat rejection from an entire cell as a singular entity, rather than requiring a cross-sectional area dimension. This allows two geometrically dissimilar cells to be directly compared using the CCC, which would not be the case using the Biot number, thermal conductance or thermal resistance, without first accounting for differing cross-sectional areas through which heat is conducting and disregarding the effects of varying topologies of, for example, the tabs.

Cell cooling coefficient in application.—The CCC_{tot}, as a standardisation of a specific cell's ability to dissipate heat, can become a valuable tool for battery pack design. An example to analyze the performance of LIB A against LIB B for a specific battery pack application is introduced. Table VII summarises the key parameters of LIB A and LIB B which includes the CCC_{tot} metric, essential for the down-selection process.

For this example, all heat generated by the individual cells in the respective packs must be removed through the tabs. The pack is required to have a 15Ah capacity, and must be capable of a continuous 4C discharge, which is within the manufacturer specification for both cells. The peak operating temperature, $T_{cell\,max}$, of the cells in the packs is required to be kept below 40°C, a typical target for industry application. The ambient air temperature is assumed to be 20°C.

Using the apparatus introduced earlier in this study, the average rate of heat generation over the course of a 4C discharge was determined to be 4.97W for LIB A and 8.28W for LIB B. Equation 19 incorporates the CCC_{tot} and is used to determine the required thermal gradient, from $T_{cell\,max}$ to T_{tabs}. This gradient is termed $\Delta T_{cell\,max\,to\,tabs}$.

$$\Delta T_{cell\,max\,to\,tabs} = \frac{\dot{Q}_{gen}}{CCC_{tot}} \qquad [19]$$

Therefore, for LIB A:

$$\Delta T_{cell\,max\,to\,tabs} = \frac{4.97}{0.332} = 14.97°C$$

and for LIB B:

$$\Delta T_{cell\,max\,to\,tabs} = \frac{8.28}{0.204} = 40.59°C$$

Therefore, the tabs of LIB B must be kept 40.59°C below the cells' required maximum operational temperature of 40°C, and therefore must

be cooled to −0.59°C. In practical terms, a coolant loop operating below 0°C, which is 20.59°C below the ambient temperature, will require an expensive refrigeration system as well high-power components to reject that heat. In contrast, the required thermal management for LIB A is dramatically reduced. The cells tabs must be held 14.97°C below the cells' required maximum operational temperature, and therefore can be allowed to reach a maximum temperature of 25.03°C, which is 5.03°C above the ambient temperature. In this case, a much simpler thermal management system may be employed, such as an indirect liquid cooling loop which rejects heat into the surrounding air.

For this application, despite both cells operating within the C-rate limits set out by the manufacturer, and additionally being able to achieve the required current rates and capacity of the pack design, the pack designer has identified a fundamental problem with the use of LIB B. Therefore, it is entirely unusable for this application. The CCC metric has verified the suitability of LIB A for the desired battery pack. This cell will reduce the demand and the complexity of the whole thermal management system and in turn simplify the componentry requirements, and therefore cost, significantly.

It should be noted that the greater capacity of LIB B is not of benefit with regard to heat removal requirements. Although only two LIB Bs are required to reach the required pack capacity, compared to three LIB As, the heat generation rate within Pack B is still greater, 16.56W compared to 14.92W.

The CCC allows a pack designer to differentiate and downselect cells at the design stage without the need to build test packs. In turn this informs upon the complexity of the required thermal management system to maintain the given cell and pack below the required maximum operational temperature.

Table VIII summarises the results from the analytical methodology which is set out above.

Conclusions

In this paper we have identified a significant gap in information provided on specification sheets about lithium-ion batteries ability to reject heat. We present a solution to this problem, an empirically determined cell cooling coefficient (CCC, units W K^{-1}) and a method to measure it, which is proposed as a standardised metric to compare different cells, and we recommend that it is included on all cell specification sheets.

Heat rejection from cells is not typically quantified by cell manufacturers, and consequently is not an optimised parameter. Considering the effect of elevated temperatures and large thermal gradients on accelerating degradation and increasing the risk of thermal runaway, the ability to reject heat from a cell should be of equal importance to power and energy density when designing or selecting a cell. For example, there is no point designing a cell for high power if it generates too much heat for it to be effectively cooled. Uptake of this standard in industry will provide end-users with a far greater understanding of cells' thermal capabilities, and cell designers will have a quantitative metric which they can optimize, accelerating innovation in cell and system design and potentially revolutionising the lithium-ion battery industry.

The CCC describes the rate of heat transfer that will occur due to a thermal gradient from the maximum temperature of the cell and its cooled surface, when it is generating heat throughout its volume. The CCC magnitude thus characterises the conduction-limited thermal response of a given cooling method for a given cell.

A detailed description of the testing apparatus and procedures for the CCC calculation are provided. The CCC has been shown to be independent of cell heat generation rate and cell operation temperature, therefore allowing significant flexibility in measurement conditions. The consistency of the CCC as a metric was evaluated by conducting 14 tests in varying experimental parameters and using three different cells. Repeatable results demonstrate that the CCC is an empirical property of a particular lithium-ion cell and can therefore be used to describe its ability to reject heat under any operational conditions.

Table VIII. Comparison of LIB A and B, to determine suitability for application in an example battery pack.

Cell	Cell heat rate/W	$\Delta T_{cell\ max\ to\ tabs}$	Maximum T_{tabs}/°C	Cells in pack	Pack heat rate/W
LIB A	4.97	14.97	25.03	3	14.92
LIB B	8.28	40.59	−0.59	2	16.56

A particular cell will have a different CCC_x for each thermal pathway. In this study the difference between the negative and positive tabs was studied. Certain known characteristics, the larger cross-sectional area of the negative tab and the enhanced thermal conductivity of the negative current collector material for example, are evident when comparing CCC_{neg} to CCC_{pos}. For a given cell the CCC, and therefore the rate of heat rejection through the negative tab, was found to be 63.6% higher for a given thermal gradient.

The present study also sets out a worked example to demonstrate how the CCC can be used in the early stages of a battery pack design. Two cells, both capable of delivering the required current for the given application, are compared. The first is able to reject heat through its tabs at the required rate to stay within the defined operational temperature window. The second is found to be entirely unsuitable for the application, given the thermal gradient required to drive the necessary rate of heat transfer. The CCC is therefore a useful tool for systems engineers to identify and down-select cells based upon their ability to reject heat, as well as their ability to deliver the desired power, capacity, cost, or lifetime, at the preliminary design phase.

Cooling methodologies are different for different cell form factors, for example tab cooling a pouch cell is relatable but not identical to base cooling a cylindrical cell. Comparison between multiple form factors is possible using the CCC. The process, determining a thermal gradient generated across a cell when a given rate of heat is generated, remains the same. However, procedural alterations to the process for CCC derivation are anticipated, and there is an expectation that scaling the coefficient to account for the volumetric heat generation rate of the cell will improve the relevance of the proposed metric.

ORCID

Alastair Hales https://orcid.org/0000-0001-6126-6986
Laura Bravo Diaz https://orcid.org/0000-0002-0259-8590
Mohamed Waseem Marzook
https://orcid.org/0000-0003-4430-7322
Yan Zhao https://orcid.org/0000-0002-3211-6740
Yatish Patel https://orcid.org/0000-0001-7828-5315
Gregory Offer https://orcid.org/0000-0003-1324-8366

References

1. International Energy Agency, *World Energy Outlook 2018* (2018).
2. N. Lebedeva, F. Di Persio, and L. Boon-brett, *Lithium ion battery value chain and related opportunities for Europe* (2017).
3. G. Zubi, R. Dufo-lópez, M. Carvalho, and G. Pasaoglu, *Renew. Sustain. Energy Rev.*, **89**, 292 (2018).
4. T. M. Bandhauer, S. Garimella, and T. F. Fuller, *J. Electrochem. Soc.*, **158**, R1 (2011).
5. H. Liu, Z. Wei, W. He, and J. Zhao, *Energy Convers. Manag.*, **150**, 304 (2017).
6. M. R. Khan, M. J. Swierczynski, and S. K. Kær, *Batteries*, **3**, 9 (2017).
7. G. Xia, L. Cao, and G. Bi, *J. Power Sources*, **367**, 90 (2017).
8. G. Karimi and X. Li, *Int. J. energy Res.*, **37**, 13 (2013).
9. P. Arora, R. E. White, and M. Doyle, *J. Electrochem. Soc.*, **145**, 3647 (1998).
10. J. Vetter, P. Novák, M. R. Wagner, C. Veit, K.-C. Möller, J. O. Besenhard, M. Winter, M. Wohlfahrt-Mehrens, C. Vogler, and A. Hammouche, *J. Power Sources*, **147**, 269 (2005).
11. R. Spotnitz and J. Franklin, *J. Power Sources*, **113**, 81 (2003).
12. D. P. Abraham, E. M. Reynolds, P. L. Schultz, A. N. Jansen, and D. W. Dees, *J. Electrochem. Soc.*, **153**, A1610 (2006).
13. T. Waldmann, M. Wilka, M. Kasper, M. Fleischhammer, and M. Wohlfahrt-mehrens, *J. Power Sources*, **262**, 129 (2014).
14. Y. Troxler, B. Wu, M. Marinescu, V. Yu, Y. Patel, A. J. Marquis, N. P. Brandon, and G. J. Offer, *J. Power Sources*, **247**, 1018 (2014).
15. I. A. Hunt, Y. Zhao, Y. Patel, and G. J. Offer, *J. Electrochem. Soc.*, **163**, A1846 (2016).
16. Y. Zhao, Y. Patel, T. Zhang, and G. J. Offer, *J. Electrochem. Soc.*, **165**, A3169 (2018).
17. B. Wu, V. Yu, M. Marinescu, G. J. Offer, R. F. Martinez-botas, and N. P. Brandon, *J. Power Sources*, **243**, 544 (2013).
18. P. Ramadass, B. Haran, R. White, and B. N. Popov, *J. Power Sources*, **112**, 614 (2002).
19. V. Ruiz and A. Pfrang, *JRC exploratory research : Safer Li-ion batteries by preventing thermal propagation* (2018).
20. T. Waldmann, G. Bisle, S. Stumpp, M. A. Danzer, M. Kasper, P. Axmann, and M. Wohlfahrt-mehrens, *J. Electrochem. Soc.*, **162**, A921 (2015).
21. C. Y. Wang and V. Srinivasan, *J. Power Sources*, **110**, 364 (2002).
22. X. Zhang, *Electrochim. Acta*, **56**, 1246 (2011).
23. M. Xiao and S. Choe, *J. Power Sources*, **241**, 46 (2013).
24. Y. Lai, S. Du, L. Ai, L. Ai, and Y. Cheng, *Int. J. Hydrogen Energy*, **40**, 13039 (2015).
25. C. Heubner, M. Schneider, and A. Michaelis, *J. Power Sources*, **307**, 199 (2016).
26. A. N. Mistry, H. R. Palle, and P. P. Mukherjee, *Appl. Phys. Lett.*, **114**, 023901 (2019).
27. A. N. Mistry, K. Smith, and P. P. Mukherjee, *ACS Appl. Mater. Interfaces*, **10**, 28644 (2018).
28. D. Bernardi, *J. Electrochem. Soc.*, **132**, 5 (1985).
29. Y. Deng, C. Feng, J. E, H. Zhu, J. Chen, M. Wen, and H. Yin, *Appl. Therm. Eng.*, **142**, 10 (2018).
30. X. Feng, M. Fang, X. He, M. Ouyang, L. Lu, H. Wang, and M. Zhang, *J. Power Sources*, **255**, 294 (2014).
31. A. Eddahech, O. Briat, and J. M. Vinassa, *Energy*, **61**, 432 (2013).
32. C. Lin, S. Xu, and J. Liu, *Int. J. Hydrogen Energy*, **43**, 8375 (2018).
33. M. Fleischhammer, T. Waldmann, G. Bisle, B. I. Hogg, and M. Wohlfahrt-Mehrens, *J. Power Sources*, **274**, 432 (2015).
34. D. Worwood, Q. Kellner, M. Wojtala, W. D. Widanage, M. Ryan, D. Greenwood, and J. Marco, *J. Power Sources*, **346**, 151 (2017).
35. Y. Xie, S. Shi, J. Tang, H. Wu, and J. Yu, *Int. J. Heat Mass Transf.*, **122**, 884 (2018).
36. K. Shah, S. Drake, D. Wetz, J. K. Ostanek, S. P. Miller, J. M. Heinzel, and A. Jain, *J. Power Sources*, **258**, 374 (2014).
37. M. I. Ardani, Y. Patel, A. Siddiq, G. J. Offer, and R. F. Martinez-Botas, *Energy*, **144**, 81 (2018).
38. R. W. Van Gils, D. Danilov, P. H. L. Notten, M. F. Speetjens, and H. Nijmeijer, *Energy Convers. Manag.*, **79**, 9 (2014).
39. Z. Ling, F. Wang, X. Fang, X. Gao, and Z. Zhang, *Appl. Energy*, **148**, 403 (2015).
40. M. Klein, S. Tong, and J. W. Park, *SAE Tech. Pap.*, 2014-01-1866 (2014).
41. K. J. Kelly, M. Mihalic, and M. Zolot, *17th Annu. Batter. Conf. Appl. Adv.*, 247 (2002).
42. Q. Wang, B. Jiang, B. Li, and Y. Yan, *Renew. Sustain. Energy Rev.*, **64**, 106 (2016).
43. J. Xun, R. Liu, and K. Jiao, *J. Power Sources*, **233**, 47 (2013).
44. D. Chen, J. Jiang, G. H. Kim, C. Yang, and A. Pesaran, *Appl. Therm. Eng.*, **94**, 846 (2016).
45. Y. Huo, Z. Rao, X. Liu, and J. Zhao, *Energy Convers. Manag.*, **89**, 387 (2015).
46. L. W. Jin, P. S. Lee, X. X. Kong, Y. Fan, and S. K. Chou, *Appl. Energy*, **113**, 1786 (2014).
47. S. J. Bazinski and X. Wang, *J. Electrochem. Soc.*, **161**, A2168 (2014).
48. S. J. Bazinski and X. Wang, *J. Power Sources*, **293**, 283 (2015).
49. X.-F. Zhang, Y. Zhang, Y. Patel, T. Zhang, W.-M. Liu, M. Chen, G. J. Offer, and Y. Yan, *Phys. Chem. Chem. Phys.*, **19**, 9833 (2017).
50. A. Samba, N. Omar, H. Gualous, O. Capron, P. Van Den Bossche, and J. Van Mierlo, *Electrochim. Acta*, **147**, 319 (2014).
51. W. Mei, H. Chen, J. Sun, and Q. Wang, *Appl. Therm. Eng.*, **142**, 148 (2018).
52. Y. Rogers and G. Mayhew, *Work & Heat Transfer*, 4th ed., p. 524, Pearson Education Limited (1967).
53. S. J. Drake, D. A. Wetz, J. K. Ostanek, S. P. Miller, J. M. Heinzel, and A. Jain, *J. Power Sources*, **252**, 298 (2014).
54. C. Forgez, D. Vinh, G. Friedrich, M. Morcrette, and C. Delacourt, *J. Power Sources*, **195**, 2961 (2010).
55. M. Ecker, T. Tran, P. Dechent, S. Kabitz, A. Warnecke, and D. U. Sauer, *J. Electrochem. Soc.*, **162**, A1836 (2015).
56. E. Schuster, C. Ziebert, A. Melcher, M. Rohde, and H. J. Seifert, *J. Power Sources*, **286**, 580 (2015).
57. P. E. de Jongh and P. H. L. Notten, *Solid State Ionics*, **148**, 259 (2002).
58. J. Zhu, Z. Sun, X. Wei, and H. Dai, *Int. J. energy Res.*, **40**, 1869 (2016).